Analysis and Motion Control of a Centrifugal-Force Microrobotic Platform

P. Vartholomeos, *Member, IEEE*, K. Vlachos, and E. Papadopoulos, *Senior Member, IEEE*

***Abstract*—This paper presents the analysis, design and closed-loop control of a mobile microrobotic platform capable of micrometer positioning on a plane. The platform is of low cost (less than $20), can be fabricated rapidly and is made of commercially available components. Its motion is induced by centrifugal forces generated by two vibration motors installed inside the platform body. The asynchronous operation of the vibration motors is shown by simulation to result in planar motions of two degrees-of-freedom locally, with micrometer resolution. A controller has been designed to generate controlled motions using sets of motor angular velocities. A prototype has been developed and used to validate the motion principle and the controller efficacy. Open loop experiments show that the platform motion resolution is approximately 20μm while its speed is greater than 2mm/s. Closed-loop experiments demonstrate a 5μm resolution, i.e. a five-fold improvement compared to the open-loop experiments. The low cost, the rapid fabrication and the micrometer motion resolution suggest that this microrobotic platform is a promising solution for low cost microfactories, where a group of such robots performs high throughput advanced microassembly of microsystems.**

***Note to Practitioners*—The aim of this work is to increase the level of autonomy and motion flexibility in micromanipulation and microassembly tasks. Despite their nanometer resolution, current micromanipulation platforms either occupy extreme volumes with respect to their workspace or suffer from expensive and/ or bulky power and driving units that limit their effectiveness in complex cooperative tasks. The developed system is a low-cost, tetherless, fully autonomous, microrobotic platform that can perform micromanipulation and microassembly tasks, such as the cooperative fabrication of microsystems or manipulation of biological specimens, in a micro scale environment. The platform motion principle exploits the centrifugal forces generated by DC vibration motors installed in the body of a microrobot, that moves as cell phones move when they vibrate. Experiments showed that the closed loop motion resolution is 5μm. A group of such robots can be used in cooperative micromanipulation and/ or microassembly tasks in the micrometer scale.**

***Index Terms*— microrobotics, mobile robot, microassembly, vibration motor, motion control.**

Manuscript received June 15, 2012.

P. Vartholomeos is with Cardiac Surgery, Children's Hospital Boston, Harvard Medical School, Boston, MA 02115 USA, (e-mail: Panagiotis.Vartholomeos@childrens.harvard.edu).

K. Vlachos and E. Papadopoulos are with the Department of Mechanical Engineering, National Technical University of Athens, 15780 Athens, Greece, (e-mail: kostaswl@central.ntua.gr; egpapado@central.ntua.gr).

I. Introduction

Packaging and assembly cost is a major portion of the overall cost of microsystems technologies (MSTs), especially of those involving the assembly of many heterogeneous parts [1]. Extensive research has been carried out on the design and development of robotic micro-manipulators that can efficiently and cost effectively fabricate MSTs. These robots must exhibit micron motion resolution and high-resolution force-capabilities. Because of their micropositioning and micromanipulation capabilities they are called microrobots, although, to be able to impart forces sufficiently high for microassembly tasks, their size typically lies on the cm^3 scale. Existing micromanipulation is implemented using static manipulators bolted at some location in the workspace performing manipulations of nanometer resolution, at high speeds, with excellent motion stability and robustness [2]. However these micromanipulators occupy a large volume compared to the strictly confined reachable workspace and consequently do not exhibit sufficient motion flexibility to perform complex cooperative tasks. Furthermore, the uncertainty pertaining micromanipulations tasks, and the limited capabilities of visual inspection at those scales can be addressed only through cooperative manipulation. To this end a robotic system is required that possesses utra-high precision, multiple degrees-of-freedom (dof), and at the same has a large workspace. This need can be met by a group of miniature mobile microinstrumented cooperative robots. These could provide micrometer motion and high-resolution force together with virtually unlimited workspace and therefore could realize complicated cooperative strategies [3].

The key component of miniature mobile microrobots is their actuation mechanism. Conventional actuation mechanisms, such as motors and wheels, do not lend themselves to micropositioning tasks due to frictional phenomena, such as the stick-slip and Stribeck effect, and the large mechanical tolerances of the actuation mechanisms [4]. Therefore, much of the research focus has been put on the novel actuation design. Several actuation techniques have been devised based on smart materials, such as piezo-electric actuators, shape memory alloys, etc. The most popular micro-positioning motion mechanism is the stick-slip principle,

which is implemented using piezoelectric actuators [3-8]. This principle is employed by the MINIMAN micro-robot [3], and by the MiCRoN robots [5,8].

Although piezoelectric actuators are arguably the favored smart material for micro-positioning and do provide the required positioning resolution, they usually suffer from expensive and bulky power and driving units. Small-scale piezoelectric drivers and amplifiers that could be accommodated on board are custom made and thus do not allow for cost effective designs [9].

This paper presents the dynamics, design, and closed loop control of a novel tetherless autonomous mobile microrobotic platform. The microrobot is actuated by a method which exploits centrifugal forces generated by DC vibration micromotors installed inside the body of the microrobot. The detailed analysis of the actuation method for synchronous operation of the DC vibration motors and open loop motion experiments have been presented in [10, 11]. The scalability of these systems and their suitability for collective behaviors has been demonstrated in [12]. In this paper the emphasis is shifted on the analysis of asynchronous operation of the vibration motors. In addition, and for the first time, closed loop control of the microrobotic platform is implemented. The resulting closed loop motion resolution is 5μm.

The rest of the paper is structured as follows. A summary of the underlying physics of the actuation principle is presented in Section II and the platform dynamics in Section III. In Section IV the asynchronous operation of the DC vibration motors is studied and is used to generate the 2 dof planar motion of the platform. The controller is described in Section V. Open loop and closed loop control experiments are executed and evaluated in Sections VI and VII respectively.

II. Motion Principle

The underlying physics of the actuation mechanism are explained using a simplified one degree of freedom (1dof) mobile platform of mass M. The actuation mechanism employs an eccentric mass m, rotated at a constant angular speed ω_m by a platform-mounted motor, as shown in Fig. 1.

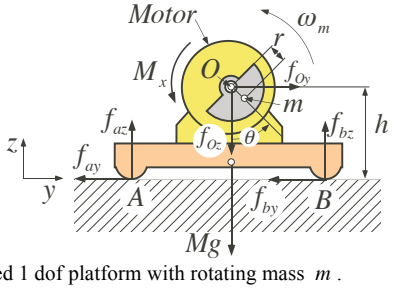

Fig. 1. Simplified 1 dof platform with rotating mass m.

The actuation angle θ defines the angular position of the eccentric mass m with respect to the vertical axis, see Fig. 1. One cycle of operation is completed when the mass m has described an angle of 360°. Gravitational and centripetal forces exerted on the rotating mass are resolved along the y-z axes to yield:

$$\begin{aligned} f_{oy} &= mr\omega_m^2 \sin\theta \\ f_{oz} &= -mg - mr\omega_m^2 \cos\theta \end{aligned} \tag{1}$$

where g is the acceleration of gravity and r is the arm of eccentricity of m with respect to O. These forces are transmitted to the platform at point O, while the small moment due to m is neglected. When the angular speed ω_m is low, the platform does not move because the horizontal actuation force f_{oy} is cancelled by frictional forces at the platform contact points A and B. However, if the angular speed ω_m exceeds a critical value $\omega_{m\_critical}$, then f_{oy} overcomes the support point friction forces, and as a result, the platform begins to slide.

Using a simplified static-kinetic friction model, the motion of the platform along the y and z-axes is described by,

$$\begin{aligned} M\ddot{y} &= f_{oy} - f_{fr} \\ 0 &= f_{az} + f_{bz} + (-Mg + f_{oz}) \end{aligned} \tag{2}$$

where all forces are defined in Fig. 1, and f_{fr} is the friction force. Neglecting viscous friction, f_{fr} is given by,

$$f_{fr} = \begin{cases} f_C \operatorname{sgn}(\dot{y}), & \dot{y} \neq 0 \\ f_{oy}, & \left\|f_{oy}\right\| < f_C, \ \dot{y} = 0, \quad \ddot{y} = 0 \\ f_C \operatorname{sgn}\left(f_{oy}\right), & \left\|f_{oy}\right\| > f_C, \ \dot{y} = 0, \quad \ddot{y} \neq 0 \end{cases} \tag{3}$$

where f_C is the Coulomb friction level, i.e. the maximum friction force that can exist for the current normal force, and is given by,

$$f_C = \mu(f_{az} + f_{bz}) = \mu(Mg - f_{oz}) \tag{4}$$

The parameter μ is the coefficient of kinetic friction and the function $\operatorname{sgn}(\dot{y})$ is defined by,

$$\operatorname{sgn}(\dot{y}) = \begin{cases} +1, & \dot{y} > 0 \\ 0, & \dot{y} = 0 \\ -1, & \dot{y} < 0 \end{cases} \tag{5}$$

The forces acting on the platform are given by Eqs. (1), (3) and (4) and are plotted in Fig. 2 for three consecutive cycles.

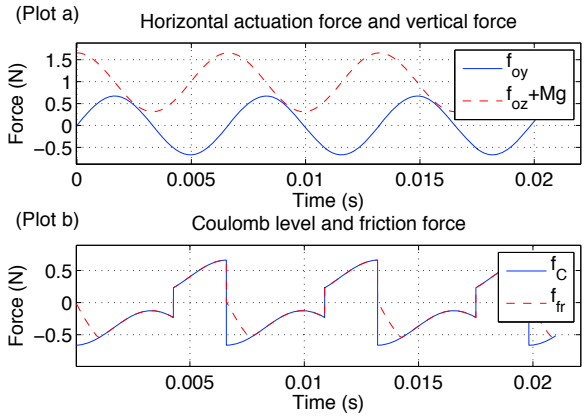

Fig. 2. (a) Horizontal and (b) vertical forces acting on a 1 dof platform.

It is observed that the horizontal actuation force f_{oy} and the vertical actuation force f_{oz} are time periodic and f_{oz} leads f_{oy} by $\pi/2$ (Fig. 2a).

Due to Eq. (4), the Coulomb friction level f_C is periodic too and in phase with f_{oz}, but its sign changes from positive to negative depending on the speed direction (Fig. 2b). This figure also shows the friction force f_{fr}. The platform's motion response caused by the forces in Fig. 2 is computed by numerical integration of Eq. (2) and is presented in Fig. 3.

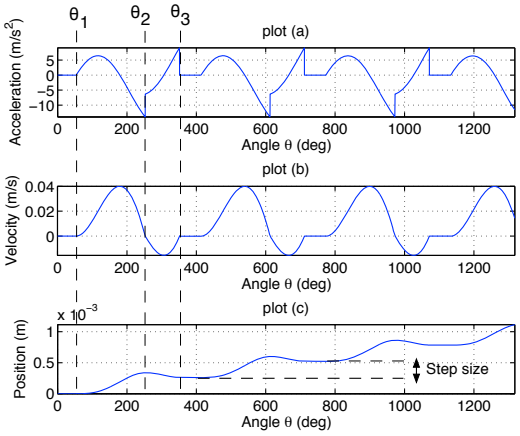

Fig. 3. Platform motion: (a) acceleration, (b) velocity and (c) position, corresponding to the forces of Fig. 2.

The physics of the motion principle are explained next in more detail. Due to (1), when the actuation angle θ is small, the actuation force f_{oy} is not sufficient to overcome the Coulomb level and no motion is induced. At a critical angle θ_1, the actuation force f_{oy} overcomes the static friction limit f_C, and motion is induced (Fig. 3). The platform executes forward motion. When m passes the highest point at $\theta = 180°$, the platform already has a positive velocity. As m moves past this point, friction forces together with actuation forces decelerate the platform. As friction still increases, it eventually brings the platform to a stop at a critical angle θ_2 (Fig. 3). The actuation forces are now pointing to the left and as a result reverse platform motion starts. While m rotates to the forth quadrant of the actuation cycle, the reverse platform motion decelerates and eventually stops at critical angle θ_3 (Fig. 3).

Quite interestingly, as shown in Fig. 3c, for a counterclockwise rotation of the eccentric load, the platform exhibits a net displacement along the positive y-axis. This is due to the fact that during platform forward motion, the eccentric mass is at the higher points of its trajectory (second quadrant of actuation cycle) and therefore the normal forces and the frictional forces are low, whereas during the reverse motion, the mass is at the lower points of its trajectory (fourth quadrant of actuation cycle) and the frictional forces are high. Consequently, the platform decelerates more during reverse motion compared to forward motion and therefore -for a counterclockwise rotation of the eccentric load- a net displacement towards the positive y-axis takes place.

III. Platform Dynamics

Two centrifugal force actuators, described in the previous section, are employed in the design of a microrobotic platform capable of two dof planar motions, see Fig. 4.

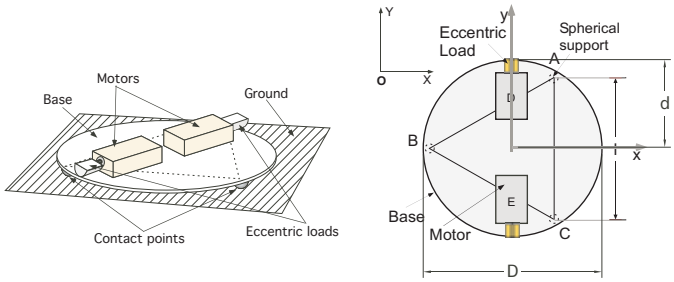

Fig. 4. The 2-actuator platform concept: (a) angle view, (b) top view.

Platform base: The contact points between the platform and the ground are provided by three fixed small steel balls A, B and C located at the vertices of an equilateral triangle (Fig. 4b). The length between the ball supports is l, while the radius of the platform base is d (Fig. 4b). The 3-contact point configuration is favored because it is not over-constrained and ensures static equilibrium along the vertical axis.

Actuators: The actuation of the platform employs miniature-vibrating motors. Each vibrating motor is axially coupled to an eccentric load, while the control input is the rotation speed ω_m of the motor. During motor rotation, the eccentric mass of the load generates periodic dynamic forces, which are transferred to the contact points and interact with the friction forces.

A. Platform dynamics

Using the Newton-Euler formulation, the platform dynamics are described by, [13]

$$M\dot{\mathbf{v}} = \mathbf{R}\sum_i {}^b\mathbf{f}_i, \qquad i = \{a,b,c,d,e\} \tag{6}$$

$$I_{zz}\ddot{\psi} = \hat{\mathbf{z}}\cdot\sum_i ({}^b\mathbf{r}_i \times {}^b\mathbf{f}_i),\ i = \{a,b,c,d,e\} \tag{7}$$

where b is the body-fixed frame, $\mathbf{R}$ is the rotation matrix between frame b and the inertial frame O (see Fig. 4b), ω_p is the platform angular velocity, and $\mathbf{v} = [\dot{x}, \dot{y}, \dot{z}]^T$ is its center of mass (CM) velocity with respect to the inertial frame O. In Eq. (7), I_{zz} is the polar moment of inertia in the body fixed frame and $\hat{\mathbf{z}}$ denotes the unit z-axis vector. In both equations the subscripts $i = \{a,b,c\}$ correspond to frictional forces at the three contact points of the platform, and $i = \{d,e\}$ correspond to the actuation forces generated by the two vibrating motors.

The actuation forces that act on the platform, when the DC micromotors rotate (assuming identical micromotors), are given by:

$$\begin{aligned} {}^b f_{ix} &= mr\ddot{\theta}_i \cos\theta_i + mr\dot{\theta}_i^2 \sin\theta_i \\ {}^b f_{iz} &= -mg - mr\ddot{\theta}_i \sin\theta_i - mr\dot{\theta}_i^2 \cos\theta_i \end{aligned} \tag{8}$$

where, $i = \{d,e\}$ and θ_i is the angle of micromotor i, m is the micromotor eccentric mass, and r is the arm of

eccentricity. The dynamics of the DC micromotor i are given by:

$$\ddot{\theta}_i = -\frac{b}{J}\dot{\theta}_i + \frac{k_t}{J} i_{Li} - \frac{mgr\sin\theta_i}{J} - \frac{c}{J}$$
$$\dot{i}_{Li} = -\frac{k_t}{L}\dot{\theta}_i - \frac{R}{L} i_{Li} + \frac{1}{L} V_{in\_i} \quad (9)$$

where, i_{Li} is the motor i current, R is the electrical resistance, b is the viscous friction, c is the Coulomb friction at the micromotor's axis, k_t is the torque constant, L is the inductance, J is the eccentric's load moment of inertia and $V_{in\ i}$ the input voltage of motor i.

IV. Platform Driving Modes

When actuators are operating at the same rotational speed, then their operation is called *synchronous*, otherwise is called *asynchronous*. When actuators operate synchronously the problem reduces to the 2D cases depicted in Fig. 5. In the first case, $\omega_{md} = \omega_{me} = \omega_m$ and $\theta_d = \theta_e = \theta$, where $\omega_{mi}, i = \{d, e\}$ are angular actuation speeds of motors D and E respectively. As a result, the centrifugal forces F_d, F_e are equal and the platform performs pure linear motion. In the second case, the motors rotate at an opposite sense, and the platform performs pure rotational motion.

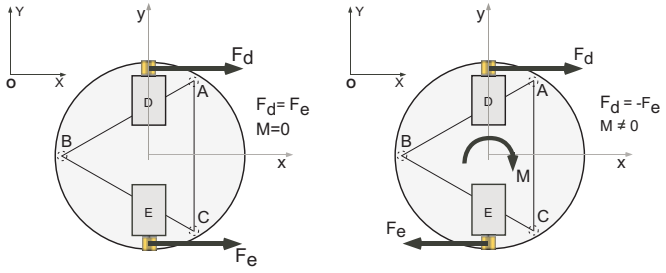

Fig. 5. Synchronous actuation: (a) pure linear, (b) pure rotational motion.

Synchronous actuation generates three distinct motion states of the platform, depending on the magnitude of the actuation forces. These are:

1. Static state: The actuation speed ω_m is smaller than a threshold value ω_{m_sl} and the resulting actuation forces are not sufficient to overcome the frictional forces at the contact points. No motion is induced.

2. Sliding state: The actuation speed ω_m is greater than the threshold value ω_{m_sl}. Actuation forces exceed the Coulomb friction level, and consequently slip of the platform occurs and motion (sliding) is induced.

3. Tipping: The actuation speed ω_m is greater than a threshold value ω_{m_tip}. The resulting actuation forces cause loss of static equilibrium along the vertical axis and tip of the platform occurs.

The three distinct motion states are delimited by the threshold actuation values $\omega_{m\_sl}, \omega_{m\_tip}$. These have been derived analytically, see [10], and are summarized in Table 1 and define the useful actuation range ω^* where $\omega_{sl} < \omega^* < \omega_{tip}$ always drives the platform in the sliding mode.

TABLE 1. Threshold values of synchronous actuation speed

	Translation	Rotation
ω_{m_sl}	$\sqrt{\frac{\mu g M}{2mr\sqrt{1+\mu^2}}}$	$\sqrt{\frac{\mu g M}{2mr\sqrt{\mu^2+\left(\frac{d}{\sqrt{2}l}\right)^2}}}$
ω_{m_tip}	$\sqrt{\frac{gM}{2mr\sqrt{1+\left(\frac{h}{\sqrt{2}l}\right)^2}}}$	$\sqrt{\frac{gM}{2mr}}$

When actuators D and E operate asynchronously, i.e. at rotational speeds ω_{md}, ω_{me}, where $\omega_{md} \neq \omega_{me}$, then the resultant actuation forces are the superposition of sinusoids of different magnitude and different frequency and form sinusoidal beats:

$$f_x(t) = A_d \sin(\omega_{md} t) + A_e \sin(\omega_{me} t) \quad (10a)$$
$$f_z(t) = -2mg - (A_d \cos(\omega_{md} t) + A_e \cos(\omega_{me} t)) \quad (10b)$$

Moments are generated about the z and x axes as described by:

$$M_z(t) = -dA_d \sin(\omega_{md} t) + dA_e \sin(\omega_{me} t) \quad (11a)$$
$$M_x(t) = dA_d \cos(\omega_{md} t) - dA_e \cos(\omega_{me} t) \quad (11b)$$

where $A_d = m_d r_d \omega_{md}^2$, $A_e = m_e r_e \omega_{me}^2$. The corresponding actuation forces and moments are depicted in Fig. 6.

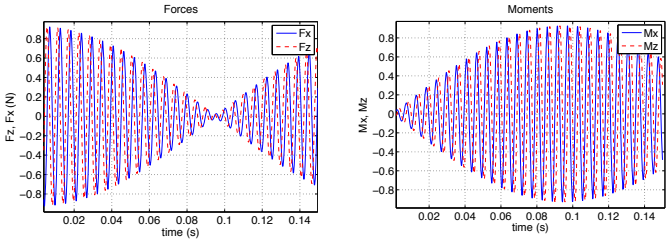

Fig. 6. Sinusoidal beat waveform: (a) actuation forces, (b) actuation moments.

The asynchronous operation of the platform is demonstrated through two simulation examples. In the first example, $\omega_{md} = 1080 rad/s$ and $\omega_{me} = 900 rad/s$, while in the second $\omega_{md} = 1060 rad/s$ and $\omega_{me} = 950 rad/s$. Both actuation sets lie within the useful actuation range ω^*, which in the case of asynchronous operation is determined numerically. The x, y, ψ motion responses are presented in Fig. 7. All three plots superimpose the motion generated by the two simulation sets. The first plot depicts the trajectories along the x-axis. The second plot depicts the angle of the platform and the third depicts the paths followed by the platform on the x-y plain.

It is observed that when $\omega_{md} = 1080\ rad/s$ and $\omega_{me} = 900\ rad/s$, the platform develops rotational speed larger compared to that when $\omega_{md} = 1060\ rad/s$ and $\omega_{me} = 950 rad/s$. On the other hand the first set results in linear speed lower compared to that of the second set. This observation is equivalent to saying that a larger difference $\omega_{md} - \omega_{me}$ results in a larger rotational speed, whereas a larger mean value $(\omega_{md} + \omega_{me})/2$ results in a larger linear

speed of the platform. Simulations have showed that this result can be generalized for any combination of actuation speeds in the useful actuation range ω^*.

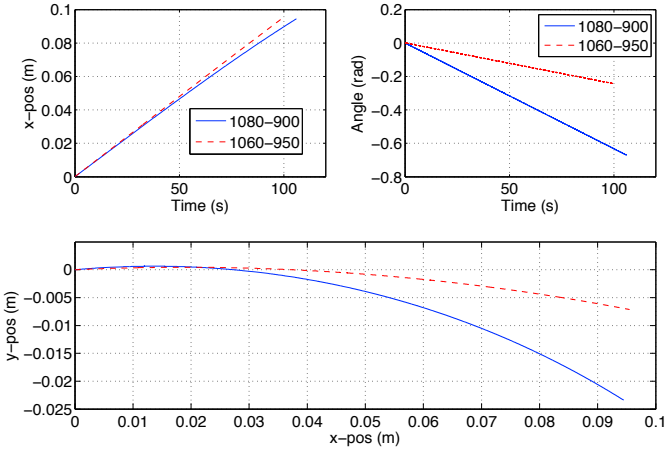

Fig. 7. Two simulation examples that demonstrate the platform response for asynchronous operation. The blue solid line represents motion due to the first set and the red dashed line represents the motion due to the second set.

Hence, we see that the asynchronous operation generates 2 dof motion using the two linearly independent control commands ~~e_1, e_2~~ ~~described by Eqs. (12) and (13).~~ At the same time, as shown in the zoom-in plots in Fig. 8, the asynchronous actuation generates successive static and kinetic phases, which correspond to the valleys and peaks of the modulating envelop of the sinusoidal beats of the actuation forces and moments. These alternating phases result in oscillatory motions (for all three motion components) that reduce the motion resolution of the platform. Hence, asynchronous operation increases the mobility of the platform from one to two dof at the expense of motion resolution.

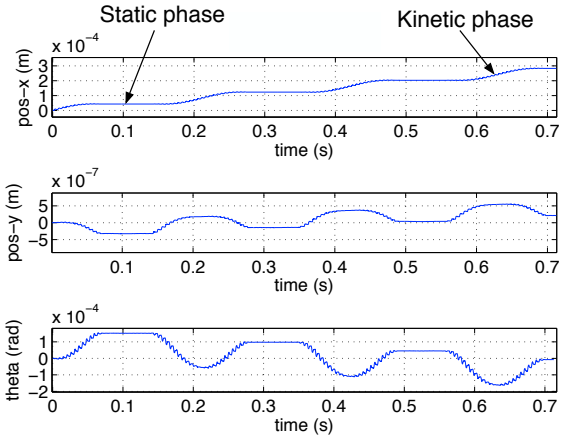

Fig. 8. Zoom in on the x, y, ψ, trajectories of the platform (first set of actuation speeds).

Next we demonstrate how asynchronous operation can be employed to compensate for undesired motion due to platform asymmetries. We consider the case where, due to asymmetry, the CM of the platform is located at a distance r = 0.002 m from the centroid and at an angle of $\varphi = 30°$ with respect to the platform body-fixed x-axis.

Fig. 9 depicts the trajectories of the asymmetric platform for the case of synchronous operation. Fig. 10 demonstrates the corrective action of the asynchronous actuation, i.e. x-translation is maintained while undesired y-translation and rotation have been reduced by one and two orders of magnitude respectively. Therefore, we see that small manufacturing asymmetries can be compensated by proper driving of the two micromotors.

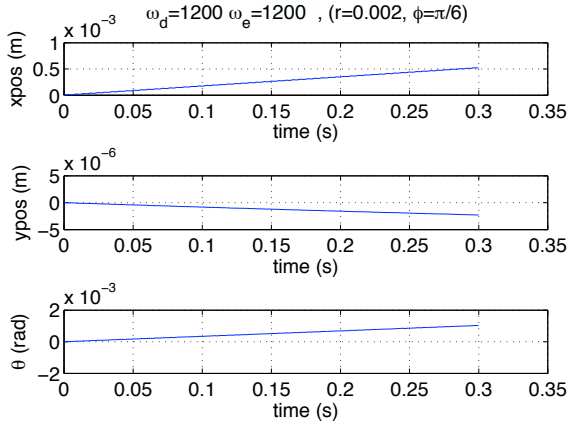

Fig. 9. Synchronous operation. The platform exhibits parasitic displacement and rotation along the y-axis and about z-axis respectively.

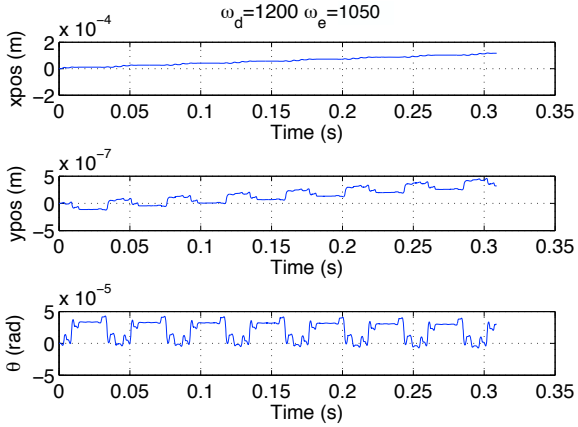

Fig. 10. Asynchronous operation compensates for the parasitic motion due to the platform asymmetry.

V. Controller Design

During a microassembly procedure, it is important ~~for a point of interest~~ of the microrobot to follow a desired path, and to reach a desired location with increased resolution. Taking into account the open-loop asynchronous behavior studied in the previous section, in this section we focus on the development of a closed-loop position controller. The ~~point of interest~~ is represented here by the endpoint of a needle mounted on the microrobot.

The aim of the controller is to force the endpoint to follow a desired path and reach a desired target point denoted by $[x_{des}\ y_{des}]^T$. Based on the platform open-loop behavior, a good choice for the system control inputs is the vector $[\omega_{md}\ \omega_{me}]^T$.

Choosing a candidate controller, a PD-type controller can be an obvious solution. However, the hardware limitations and system complexity result ~~to~~ a limited range of actuation speeds that would result often ~~to~~ controller to saturation.

To address this issue, a simple rule-based controller has been designed and described by the following set of rules:

$$\begin{bmatrix} \omega_{md} \\ \omega_{me} \end{bmatrix} = \begin{cases} [\omega_{md\downarrow} \ \omega_{me\downarrow}]^T & \text{if } y < y_{des} - \varepsilon \\ [\omega_{md\rightarrow} \ \omega_{me\rightarrow}]^T & \text{if } y_{des} - \varepsilon < y < y_{des} + \varepsilon \\ [\omega_{md\uparrow} \ \omega_{me\uparrow}]^T & \text{if } y > y_{des} + \varepsilon \end{cases} \quad (14)$$

where $[\omega_{md\downarrow} \ \omega_{me\downarrow}]^T$ and $[\omega_{md\uparrow} \ \omega_{me\uparrow}]^T$ denote motor angular velocity pairs that result in a platform displacement with a positive or negative instantaneous curvature respectively. The vector $[\omega_{md\rightarrow} \ \omega_{me\rightarrow}]^T$ denotes the pair of motor angular velocities that result in straight line translation, and 2ε designates the width of the acceptable path. The specific angular velocity pair values depend on system parameters and distance from the target, and are identified by experiments.

A graphical representation of the controller action is illustrated in Fig. 12. The colored strip represents part of the desired path. The platform is forced to translate inside the desired path strip. When the needle tip reaches the target location, both motors are stopped.

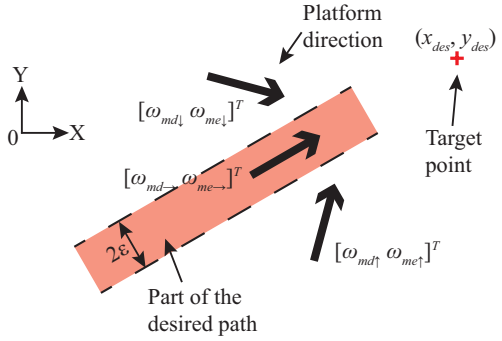

Fig. 12. Graphical representation of the proposed controller.

VI. Robot Prototype

A first microrobot prototype was built, see Fig. 13. This includes two vibration motors ~~fed~~ by pic-controlled H-bridges, wireless communications to a PC commanding station, a needle with force sensing capabilities, and an on-board battery. For more information, one can look at [12].

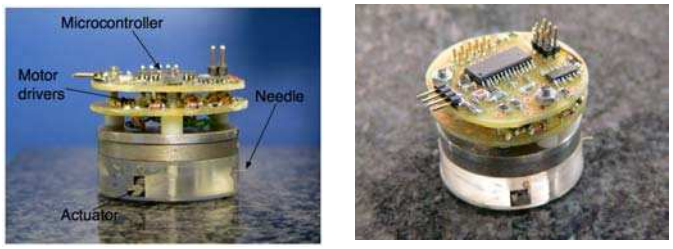

Fig. 13. Second prototype of the microrobot (a) lateral view, (b) angle view.

A second prototype has been built, see Fig. 14. This is characterized by a more compact design, and is equipped with advanced electronics, and includes additional features, such as laser displacement sensors, motor speed optical sensors, and battery recharging through a USB port. The experiments presented in the next section are realized with the first prototype, as the code for the second one is at the debugging stage.

Fig. 14. Second prototype of the microrobot (a) lateral view, (b) angle view.

The experiments are designed by taking into account a microassembly scenario. According to this, a microassembly task consists of two phases. In the first phase, the microrobotic platform executes a macroscale motion towards a target. In the second phase, the platform executes microscale motions, and the microassembly or micro-manipulation task is performed in the field-of-view of a microscope. While the first phase demands increased velocity, the second phase requires increased motion resolution.

VII. Open-Loop Experiments

In this section, the results from open loop experiments are ~~given and discussed~~. These results are used to quantify open-loop motion characteristics of the platform such as motion resolution and speed, and to understand its open-loop limitations. Furthermore, the knowledge acquired by these experiments is used to implement the closed loop control architecture presented in Section VI.

A. Macroscale translational motion.

In the macroscale experiments, the platform motion is recorded by a digital video-camera. The video file is then processed off-line by image processing routines of the Image Processing Toolbox of Matlab. To capture both position and orientation, three white circular marks were added to the top surface of the microrobot.

In the first experiment, the motors operate synchronously at $10{,}000$ *RPM* , with the same sense of rotation. The platform performs a pure translation (as described in Section IV). The open-loop synchronous operation of the motors was achieved by trial and error, i.e. the voltages producing the same speed in each motor were identified and applied. The resulting microrobot x-y plane path and trajectory are depicted in Fig. 15. Ideally, the platform should perform pure translational motion along the x-axis. In practice the platform translates along the x-axis at $1.2mm/s$, exhibiting an 8% translation along the y-axis and a 6° rotation.

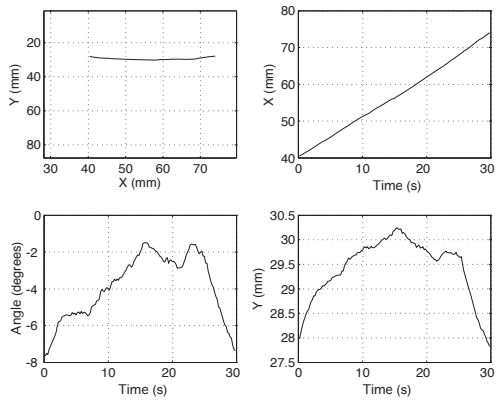

Fig. 15. Macroscale translation of platform.

The parasitic motion components are due to microrobot asymmetries, errors in actuation synchronization and non-uniform distribution of friction on the supporting surface. These ~~error sources~~ can be eliminated by closed loop control.

B. Macroscale rotational motion

The actuators operate synchronously at $10{,}000 RPM$, in an opposite sense, and the platform performs pure rotation. The path and the trajectories are depicted in Fig. 16. The platform rotates about its vertical axis at a constant speed of $0.052\ rad/s$. The platform also exhibits open-loop translational speed of approximately 0.1mm/s and 0.03mm/s along the x and y-axis respectively.

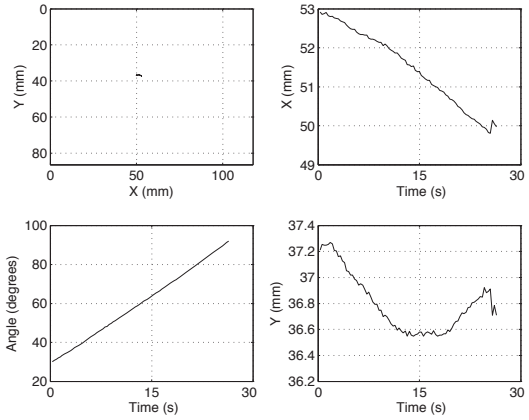

Fig. 16. Macroscale rotation of the platform.

C. Macroscale combined motion

The actuators operate asynchronously at $\omega_{md} = 10{,}000 RPM$ and $\omega_{me} = 9{,}000 RPM$. The open-loop motor speeds were achieved by trial and error, where voltages producing the desired speed at each motor were identified and applied. The path and trajectories of the platform are depicted in Fig. 17. The microrobot performs a curvilinear motion on the x-y plane. The corresponding simulation in Section IV has predicted similar trajectories.

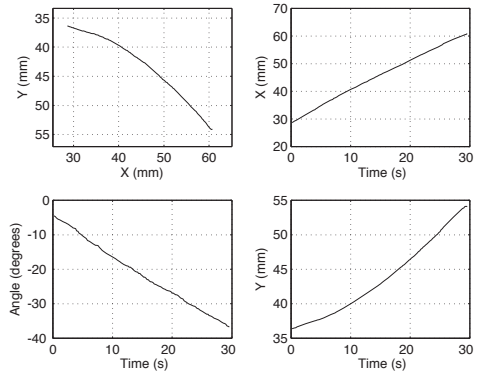

Fig.17. Macroscale combined motion.

D. Microscale translational motion

The microscale motion of the platform is measured by following the trajectory of the tip of the needle mounted on the platform. The needle tip motion is recorded by a video-microscope, which has a maximum field of view of $1 mm^2$ and a minimum field of view of 330 μm^2. The video camera pixel size was chosen so that the measurement resolution of the system is approximately 2μm. The video camera selected was the Marlin F146B, from Allied Vision Technologies, GMBH.

The actuators operate synchronously at a speed of 7,000 RPM and at the same sense of rotation. The microrobot motion response is depicted in Fig. 18. It moves for 215 μm along the x-axis at a speed of 8 μm/s. The microrobot needle tip exhibits undesired translation of 30 μm along the y-axis, which is due to a 2×10^{-3} rad/s angular oscillation of the microrobot about its CM.

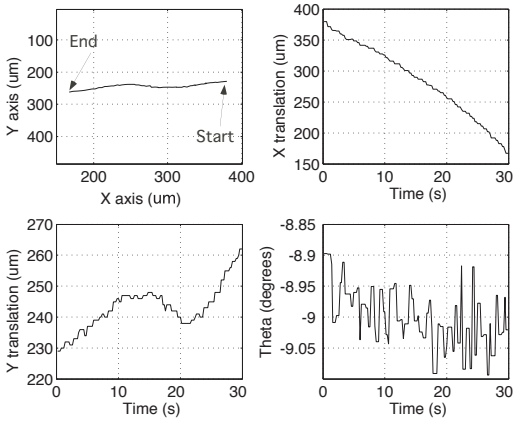

Fig.18. Microscale translation: Translation and rotation of the micro-needle tip within the field of view of the microscope.

The angular oscillation is due to synchronization errors of the actuators. The actual y-translation of the CM of the platform is estimated to be less than 5 μm. When the actuation command is set to zero (stop command) the platform exhibits a transient response, during which it covers a distance of up to 5 μm. Incorporating all sources of error leads to an open-loop translational microrobot motion resolution approximately 20μm.

VIII. Closed-Loop Control Experiments

This section presents a set of experimental closed loop position results. As mentioned earlier, the second phase of the microassembly scenario requires increased motion resolution. This can be achieved using the controller of Section V. ~~To validate the controller~~, a number of closed-loop microscale translational motion experiments were conducted. The goal for the microrobot-mounted needle tip is to follow a predefined horizontal corridor-like path of width 2ε, reach a desired target point, and then stop.

While the needle tip motion is recorded by the same video-microscope as in the open-loop microscale experiments, here the images are transmitted via a FireWire 400 port to a Core 2, 2.00 GHz PC laptop, and processed on-line in Matlab. The outcome of the image processing of each frame is the plane position of the needle tip. This information is fed back to the controller, and the control inputs are calculated, according to Section V. The inputs, expressed as PWM commands, are transmitted wirelessly to the microrobot and the appropriate voltages are applied to its motors. The control loop duration is less than 10 ms.

Table 2 summarizes the needle tip coordinates of the Start, the End point, and the Target point. As shown in Fig. 19a, the needle tip begins its motion at the Start point. After 4.32 s it reaches the desired path strip and remains in it, moving towards the Target point. From Fig. 19b, it can be seen that the position error along the X and Y axes is 2.4 μm and 4.8 μm respectively. The needle tip trajectories along the X and Y axes are depicted in Fig. 19c and Fig. 19d. The orientation of the tip is shown in Fig. 19e. The commanded angular velocities of the motors are expressed as PWM control values and are presented in Fig 19f. Table 3 summarizes the controller parameters. The variation of the PWM control values observed at the end of the experiment is due to the position measurement noise from the camera.

TABLE 2. START, END, AND TARGET POINT COORDINATES

	X coordinate (μm)	Y coordinate (μm)
Start point	541.5	698.1
End point	1350.6	562.8
Target point	1353	558

TABLE 3. CONTROLLER PARAMETERS FOR ε = 50 μm

ω_{md}	PWM %	ω_{me}	PWM %
$\omega_{md\downarrow}$	39 %	$\omega_{me\downarrow}$	31 %
$\omega_{md\rightarrow}$	35 %	$\omega_{me\rightarrow}$	33 %
$\omega_{md\uparrow}$	32 %	$\omega_{me\uparrow}$	36 %

As shown by this and other experiments, closed-loop position control yields a 5μm resolution, i.e. a five-fold improvement compared to open-loop operation. The position errors are due mainly to steady-state motor speed discrepancies and to the slow motor speed transient response. It is expected that the addition of motor speed control will reduce further the position error due to an increase in the actuator bandwidth. The experimental results described here are supported by a video, which is submitted with this paper.

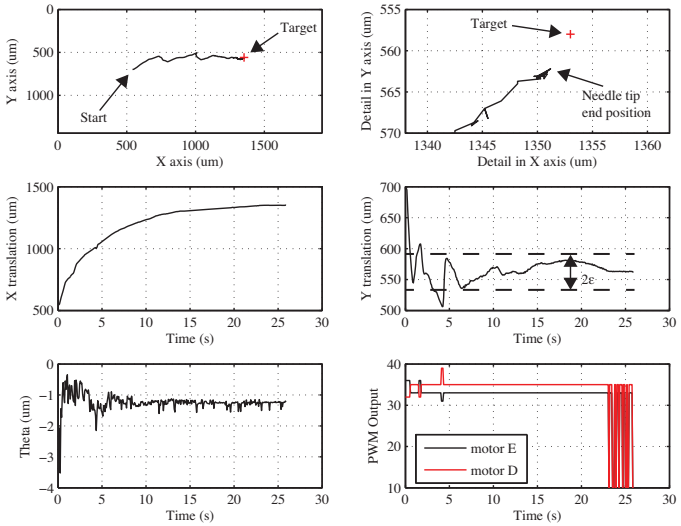

Fig. 19. Microscale positioning experiment: (a) path of the micro-needle tip, (b) zoom in on the end position of the micro-needle tip, (c) x trajectory of the tip, (d) y trajectory of the tip, (e) θ trajectory of the tip, (f) PWM output from the controller.

IX. Conclusions

This paper presented the analysis, design and closed-loop control of a mobile microrobotic platform capable of micrometer positioning on a plane. The platform is of low cost (less than $20), can be fabricated rapidly and is made of commercially available components. The microrobot motion is induced by centrifugal forces generated by two DC vibration motors installed inside the platform body. The dynamic model of the microrobot platform was developed to predict its motion. Using this dynamic model, the synchronous and asynchronous driving principles were analyzed, simulated and evaluated. The synchronous driving principle provides 1dof planar motions of high resolution, either a pure translational or a pure rotational. The asynchronous operation provides 2dof motion, but the resulting motion resolution is lower than that of the synchronous operation due to the sinusoidal beat behavior. A controller has been designed to generate controlled planar motion of the platform using a set of rules. Open loop experiments demonstrated that the motion resolution of the microrobot prototype is approximately 20μm and its speed is greater than 2mm/s. Closed-loop experiments (where the loop closes at the platform position) demonstrated a 5μm motion resolution, i.e. five-fold improvement compared to the open-loop experiments. Due to their characteristics, a group of such microrobots can be used in cooperative micromanipulation and/ or microassembly tasks in the micrometer scale.

ACKNOWLEDGMENTS

The authors wish to thank C. Dimitropoulos for his assistance in the realization of the experiments, and A. Nikolakakis for building the second prototype microrobot.

REFERENCES

[1] Sergej Fatikow, Ulrich Rembold, Microsystem Technology and Microrobotics, *Springer; 1 edition (February 12, 2002).*

[2] Y. Sun and B. J. Nelson, "Microrobotic cell injection," *IEEE Int. Conf. Robotics and Automation*, Seoul, Korea, 2001, pp. Vol. 1, pp. 620-625.

[3] Schmoeckel, F., and Fatikow, S, "Smart Flexible Microrobots for Scanning Electron Microscope (SEM) Applications," *Journal of Intelligent Material Systems and Structures*, Vol. 11, No. 3, 2000, pp. 191-198.

[4] Dario, P., Valleggi, R. Carrozza, M.C., Montesi, M.C. and Cocco, M. "Microactuators for Microrobots: A critical Survey," *Journal of Micromechanics and Microengineering*, vol. 2, 1992, pp. 141-157.

[5] J. Brufau, M. Puig-Vidal, et. al, "MICRON: Small Autonomous Robot for Cell Manipulation Applications", *Proc. of the IEEE International Conference on Robotics & Automation*, Barcelona, Spain, April 18-22, 2005, pp. 844-849.

[6] A. Bergander, W. Driesen, A. Lal, T. Varidel, M. Meizoso, H. Bleuler and J.-M.Breguet, "Position Feedback for Microrobots based on Scanning Probe Microscopy," *IEEE/RSJ International Conference on intelligent Robots and Systems* (IROS2004), Sendai, Japan, 28 Sept.-2 Oct 2004, Vol. 2, pp. 1734 - 1739.

[7] Martel S. and Hunter I., "Nanofactories based on a fleet of scientific instruments configured as miniature autonomous robots," Journal of Micromechatronics, Vol. 2, No. 3-4, pp. 201-214, 2004.

[8] Anh Tuan Nguyen and Sylvain Martel, "Locomotion of a Miniature Robot Based on Synchronized Vibrating Actuation Mechanisms," *IEEE/ASME Advanced intelligent Mechatronics, 2007 (AIM07),* 4-7 Sept, Zurich, Switzerland, pp. 1-6.

[9] M. Karpelson, G.-Y. Wei, and R.J. Wood, J., "Driving high voltage piezoelectric actuators in microrobotic applications", Sensors and Actuators A: Physical, 2011.

[10] P. Vartholomeos and E. Papadopoulos, "Dynamics, Design and Simulation of a Novel Microrobotic Platform Employing Vibration Microactuators," *Journal of Dynamic Systems, Measurement and Control*, ASME, Vol. 128, pp. 122-134, March 2006.

[11] P. Vartholomeos and E. Papadopoulos, "Analysis, Design and Control of a Planar Micro-robot Driven by Two Centripetal-Force Actuators", International Conference on Robotics and Automation (ICRA 2006), 15-19 May 2006, Orlando, Florida US, p. 649-654.

[12] Michael Rubenstein, Christian Ahler, Radhika Nagpal, "Kilobot: A Low Cost Scalable Robot System for Collective Behaviors", IEEE Intl. Conf on Robotics and Automation (ICRA), 2012.

[13] L. Sciavicco and B. Siciliano, "Modelling and Control of Robot Manipulators," Springer 2003.